Batteries & Supercaps

Research Article
doi.org/10.1002/batt.202300522

Chemistry Europe
European Chemical Societies Publishing

www.batteries-supercaps.org

Influence of Electrode Structuring Techniques on the Performance of All-Solid-State Batteries

Moritz Clausnitzer,*[a, b] Timo Danner,*[a, b] Benedikt Prifling,[c] Matthias Neumann,[c] Volker Schmidt,[c] and Arnulf Latz[a, b, d]

All-solid-state batteries (ASSBs) offer a promising route to safer batteries with superior energy density compared to conventional Li-ion batteries (LIBs). However, the design of the composite cathode and optimization of the underlying microstructure is one of the aspects requiring intensive research. Achieving both high energy and power density remains challenging due to limitations in ionic conductivity and active material loading. Using structure-resolved simulations, we investigate the potential of perforated and layered electrode designs to enhance ASSB performance. Design strategies showing significant performance increase in LIBs are evaluated regarding their application to ASSBs. Composite cathodes with solid electrolyte channels in the structure do not significantly increase cell performance compared to unstructured electrodes. However, the design with a two-layer cathode proves promising. The layered structure effectively balances improved ionic transport due to increased solid electrolyte fraction at the separator side and substantial active material loading through increased active material fraction at the current collector side of the cathode. Our research highlights key challenges in ASSB development and provides a clear direction for future studies in the field.

Introduction

Electric vehicles (EVs) are an essential component for the decarbonization of the transport sector. The battery chemistry and its corresponding properties substantially influence their environmental impact, cost, and social acceptance.[1–3] The weight and efficiency of EVs are directly affected by battery mass. Therefore, lightweight battery cells with high specific energy are of paramount importance for electric vehicles.[4] Additionally, fast charging is a strict requirement for widespread EV adoption, emphasizing the need for cells with high power density.[5,6]

Owing to their high energy and power density, Li-ion batteries (LIBs) are the preferred choice for mobile applications.[4] Over the past decade, LIBs have made tremendous progress, achieving energy densities exceeding 250 Wh/kg and allowing fast charging to 80% state of charge (SOC) in under 30 minutes.[7–9] However, additional progress is needed to accelerate the increase in the number of electric vehicles.

A promising technology to increase battery performance and safety are all-solid-state batteries (ASSBs) with a solid Li-ion conducting electrolyte (SE). ASSBs can potentially enable Li-metal anodes, significantly increasing the achievable volumetric and gravimetric energy density.[10] However, ASSBs still face several limitations. These include stability issues, high charge transfer resistances at the numerous solid-solid interfaces, insufficient ionic conductivity of the SE, and non-optimized cathode design.[11,12]

The energy and power density of an ASSB are strongly influenced by the cathode, which is typically a composite structure composed of SE and cathode active material (CAM) particles, forming interconnected clusters.[13] For superior performance, both the effective ionic conductivity in the SE phase and the electronic conductivity in the CAM phase must be sufficiently high. Furthermore, achieving a high energy density necessitates thick cathodes and substantial CAM loading.[11] However, increased CAM fractions lead to increased effective tortuosity[1] in the SE phase and low effective ionic conductivity.[15] This is critical at high cathode thickness and elevated current densities, where ionic limitations can lead to poor CAM utilization.[16] So far, enabling both high energy and power density in ASSBs is prevented by either low CAM loading or insufficient effective ionic conductivity of the composite cathode.[17,18]

[a] M. Clausnitzer, Dr. T. Danner, Prof. Dr. A. Latz
German Aerospace Center (DLR),
Institute of Engineering Thermodynamics
Pfaffenwaldring 38–40, 70569 Stuttgart (Germany)
E-mail: moritz.clausnitzer@dlr.de
timo.danner@dlr.de

[b] M. Clausnitzer, Dr. T. Danner, Prof. Dr. A. Latz
Helmholtz Institute Ulm for Electrochemical Energy Storage (HIU)
Helmholtzstraße 11, 89081 Ulm (Germany)

[c] Dr. B. Prifling, Dr. M. Neumann, Prof. Dr. V. Schmidt
Ulm University, Institute of Stochastics
Helmholtzstraße 18, 89081 Ulm (Germany)

[d] Prof. Dr. A. Latz
Ulm University, Institute of Electrochemistry
Albert-Einstein-Allee 47, 89081 Ulm (Germany)

Supporting information for this article is available on the WWW under https://doi.org/10.1002/batt.202300522

[1] In this article, we generally refer to the effective tortuosity. For an overview of the various types of tortuosity and their respective definitions, see Ref. [14].

Research Article
doi.org/10.1002/batt.202300522

An essential requirement for high effective ionic conductivity in energy-dense cathodes is a high bulk conductivity of the SE.[11] Furthermore, the microstructure significantly impacts charge transfer within the composite cathode. Recently, experimental and simulation studies have focused on optimizing composite cathode microstructure for improved cell performance.[15–25]

Ionic conductivity in the cathode can be increased by reducing effective tortuosity in the SE phase. An effective way for reducing tortuosity in the SE is to increase SE fractions in the cathode.[15,19,22] However, this comes at the cost of diminished CAM fractions, resulting in a reduced energy density. Moreover, cathode void volume must be minimized, as voids lead to limitations of ionic transport, especially at elevated CAM fractions.[19,26] Tortuosity in the SE phase is also influenced by the size of SE and CAM particles. Minimum effective tortuosities are achieved for large CAM and small SE particles.[13,27,28] However, a high ratio between CAM and SE particle size can lead to transport limitations due to a higher number of grain boundaries in the SE and longer diffusion pathways in the CAM.[19,20,29,30]

These considerations impose inherent trade-offs, limiting the potential of structural optimization of homogeneous composite cathodes for improved cell performance. However, electrode structuring techniques can address some constraints in homogeneous cathodes. Introducing specific inhomogeneities in the microstructure can improve the effective ionic conductivity while maintaining high CAM loading, aiming for both high power and energy density. However, the development of such concepts for ASSBs has been rarely reported in the literature.

In recent years, perforated electrodes have emerged as a promising strategy to enhance charge transfer in conventional LIBs.[31–40] Perforations in the electrodes, typically induced via laser processing, are infiltrated by the liquid electrolyte (LE), providing direct channels for fast ionic transport through the electrode. Perforated electrodes effectively reduce concentration gradients, improving ionic transport and thus enabling better cell performance at elevated currents.[39] Similarly, multilayer coatings were suggested to enhance ion transport in the porous electrodes, providing higher power density.[41–44] Transfer of these approaches to ASSBs might be a viable pathway towards improved cell performance.

Recently, Rosen et al. presented a novel layered cathode design, layering three distinct composite compositions using tape casting.[45] By increasing the SE fraction at the separator side of the cathode, the ionic transport in the cathode can be improved. At the same time, an increased CAM fraction at the current collector side ensures high CAM loading and good electronic transport. The layered cathodes showed better cell performance than homogeneous cathode structures at low experimental current densities. Bielefeld et al. used structure-resolved simulations to investigate the potential advantages of a cone-like cathode structure for ASSBs.[25] In their simplified model geometries, the SE fraction decreases continuously from separator to current collector, leading to a moderate decrease in overpotential compared to an unstructured electrode.

While there has been increasing interest in structuring techniques for ASSBs, a comprehensive study is still missing in the literature. In a recent study, we employed 3D continuum simulations to examine the effect of cathode composition, particle size, and cathode density on the electrochemical cell performance of homogeneous ASSB composite cathodes.[19] Building on this, the current work applies the same structure-resolved simulation approach to investigate the benefits of cathode structuring on cell performance. We investigate a perforated and two-layer cathode concept, which can potentially mitigate ionic transport limitations in high-energy electrodes. Our simulation approach focuses on the correlations between cathode microstructure and electrochemical cell performance, enabling us to identify optimal configurations. We simulate LIB and ASSB scenarios to show the material-dependent requirements for an optimum microstructure. With our physics-based simulation approach, we aim to provide guidelines for future developments.

Simulation Methodology

Simulation workflow

We use structure-resolved simulations to explore the influence of electrode structuring techniques on the electrochemical cell performance of ASSBs. Figure 1 provides an overview of the simulation workflow. Initially, we generate virtual microstructures that serve as the input for our 3D simulations. We focus on two sets of structures: Cells with a perforated and layered cathode design. For the perforated cathodes, we vary the perforation size. For the layered design, we focus on a two-layer concept, adjusting the individual layer thickness. This approach allows us to identify optimum configurations for specific operating conditions. In our simulations, we consider the active material $LiNi_{0.8}Mn_{0.1}Co_{0.1}O_2$ (NMC811) and the solid electrolyte Li_6PS_5Cl. Additionally, we simulate the corresponding structuring concepts in LIBs, serving as a reference. By evaluating and comparing our simulation results, we identify limiting processes and show the potential benefits of electrode structuring techniques for ASSBs.

A detailed description of the simulation framework and material parameters is given in Section 'Computational Section'.

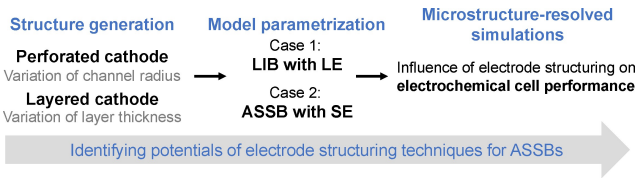

Figure 1. Simulation workflow for investigating the impact of electrode structuring techniques on the electrochemical cell performance for ASSBs.

Research Article
doi.org/10.1002/batt.202300522
Chemistry Europe
European Chemical Societies Publishing

Structure generation

For this study, we generate virtual microstructures of a perforated and layered cathode design. Details on the stochastic 3D structure generator, calibrated to the microstructure of conventional LIB cathodes, for homogeneous electrodes with different electrode density and particle size are provided in Ref. [46]. To facilitate a direct comparison between LIBs and ASSBs, we maintain a consistent cathode structure in both cases by using the generated structures for LIB and ASSB simulations. However, for the ASSB simulations, the CBD phase in the structures is fully substituted by SE, representing binder-free electrode concepts.[47,48] In all cases, the area-specific theoretical capacity of our reference structure is approximately 7 mAh/cm^2, and the structuring concepts reduce the theoretical capacity. The voxel-based structures are used as input for our electrochemical model, enabling direct correlation between microstructure and electrochemical cell performance.

Perforated cathodes

Perforated electrodes are commonly manufactured with a symmetric pattern of holes throughout the electrode. In LIBs, the LE wets the channels, facilitating fast ion transport. Due to the symmetric hole pattern, these structures can be efficiently modeled using representative geometries that consider quarter holes and apply isolating boundary conditions.[34,37,39] This approach is depicted in Figure S1(a).

We use a homogeneous cathode microstructure with a CAM fraction of 65 vol%, an electrolyte fraction of 14 vol%, and a carbon binder domain (CBD) fraction of 21 vol%. The generated structure has a size of 106×60×60 μm (x/y/z), with the x-axis oriented towards the current collector. We then introduce electrolyte channels into the structure by substituting CAM and CBD voxels with electrolyte up to a specific radius, simulating the desired perforation pattern. Dimensions in the y and z directions are the distance between hole centers in this symmetric simulation setup. Figure 2(a) displays the cross-section of the generated cathode structures, characterized by the channel radius $r_{channel}$. We vary $r_{channel}$ between 0 and 36 μm,

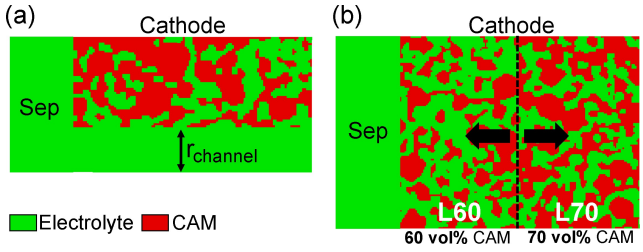

Figure 2. Generated cathode microstructures for the ASSB case. (a) Cross-sectional view of a perforated cathode with a variable channel radius between 0 and 36 μm. (b) Cross-sectional view of a layered cathode with a first layer containing 60 vol% CAM at the separator side, and a second layer with 70 vol% CAM at the current collector side. While the overall thickness of the cathode is held constant, individual layer thickness is varied.

leading to a reduction of up to 28% of the CAM fraction relative to the original structure.

Layered cathodes

We investigate a two-layer concept as a basic representation of a wider spectrum of structuring strategies, ranging from multi-layer designs to gradient configurations.[45] These strategies aim to improve cell performance by increasing the CAM fraction across the cathode length from the separator to the current collector. In our two-layer configuration, the first layer L_{60} at the separator side of the cathode, has a CAM fraction of ≈60 vol%. At the current collector side, the second layer L_{70} contains an increased CAM fraction of ≈70 vol%. The layer with 70 vol% CAM possesses a high CAM loading while maintaining a percolating network in the electrolyte phase. Reducing the CAM fraction to 60 vol% (L_{60}) significantly enhances the effective ionic conductivity at still a substantial CAM fraction.[15,19] To assess the potential of the two-layer design in enhancing cell performance, we adjust the thickness of each layer, denoted by d_{L60} and d_{L70}, respectively, while maintaining a constant overall cathode thickness.

For the simulation study in the present paper, we vary the layer thickness fraction f_{L60}, which represents the ratio of the thickness of layer L_{60} to the overall cathode thickness:

$$f_{L60} = \frac{d_{L60}}{d_{L60} + d_{L70}} \quad (1)$$

We generate the layered structures starting from two homogeneous structures with approximately 60 and 70 vol% CAM that serve as reference points for our simulations. From these structures, we derive the layers L_{60} and L_{70}, which are subsequently stacked based on the specific configuration. Figure 2(b) illustrates our generated structures in a cross-section, while Figure S1(b) shows an exemplary 3D structure. The size of the generated structures is 100×80×80 μm.

Virtual cell assembly

To generate the input geometry for our simulations, we add a planar anode, separator, and current collectors to the cathode structures. An overview of the simulation geometries is shown in Figure S2.

Results and Discussion

This study uses structure-resolved simulations to determine the potential of a perforated and a two-layer cathode design for improved cell performance. Relevant performance indicators, such as capacity or energy density, are defined in the supporting material. For each design strategy, we provide an overview of the impact of the cathode structuring on theoret-

Research Article
doi.org/10.1002/batt.202300522
Chemistry Europe
European Chemical Societies Publishing

ical capacity and ionic conductivity. From our simulation results, we identify limiting processes and optimal structures.

Perforated cathodes

Overview

As described in Section Structure generation, we generate perforated structures with varying channel radius between 0 and 36 μm. These perforations are completely filled with electrolyte, providing channels for ionic transport. Increasing the channel radius leads to reduced effective tortuosity in the electrolyte phase and higher effective ionic conductivity. However, the CAM fraction in the cathode is reduced, resulting in a decrease in theoretical capacity.

Figure 3 highlights the influence of the channel radius on both normalized effective ionic conductivity and normalized theoretical capacity. The normalized effective ionic conductivity relates the effective ionic conductivity of the microstructures to the bulk ionic conductivity of the electrolyte. Therefore, it is independent of material parameters. As the channel radius increases, the theoretical capacity drops significantly. For the largest channel radius, it reduces to 72 % of the capacity of the unstructured cathode. However, larger channel diameters significantly increase effective ionic conductivity, owing to the reduced effective tortuosity in the electrolyte phase. Therefore, ionic transport limitations are mitigated.

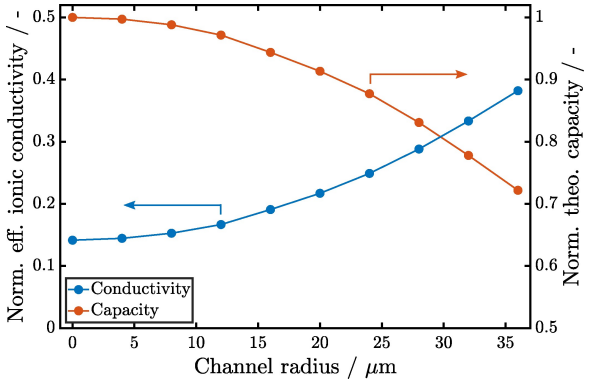

Figure 3. Effect of channel radius on effective ionic conductivity and theoretical capacity. The effective ionic conductivity is normalized with the bulk conductivity of the electrolyte. The theoretical capacity is normalized by the theoretical capacity of the structure without perforation.

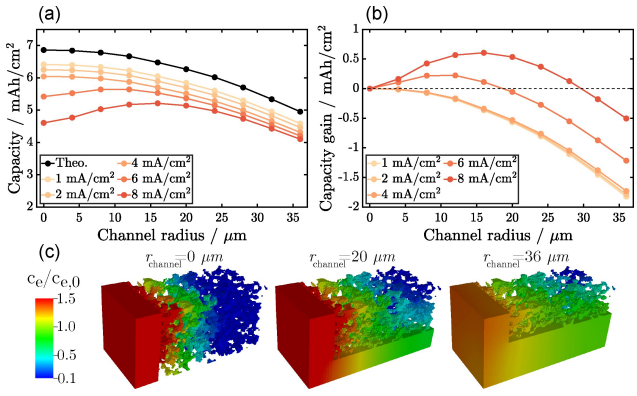

Figure 4. Effect of channel radius on electrochemical cell performance for the LIB case. (a) Practical capacity for various current densities. The black line represents the theoretical capacity of structures with channels. (b) Capacity gain of perforated structures at varying current density compared to the non-perforated structure ($r_{channel}$ = 0 μm). (c) Normalized Li-ion concentration in the electrolyte phase within the separator and cathode for increasing channel radius at 8 mA/cm².

Electrochemical cell performance

LIB case

We first conduct simulations for a LIB with LE to demonstrate the potential advantages of a perforated cathode design. Figure 4(a) shows the simulated capacities for varying channel radius at current densities between 1 and 8 mA/cm². The theoretical capacity, depicted with the black curve, decreases with increasing channel radius due to the lower CAM loading. Due to transport limitations, elevated current densities lead to higher overpotentials and decreasing capacities. However, larger electrolyte channels mitigate these transport limitations. At higher current densities, these channels have an increasingly positive effect on capacity.

Figure 4(b) shows the capacity gain of the cathodes with channels compared to the homogeneous reference ($r_{channel}$ = 0 μm). At low current densities, kinetic limitations are minimal, resulting in almost full CAM utilization. Due to the lower theoretical capacities, larger channels lead to decreasing capacities. However, as current density increases, kinetic limitations become more significant. Insufficient ionic transport can cause reduced CAM utilization across the cathode thickness, posing a considerable challenge for high-energy-density cathodes.[49,50] Significant concentration gradients can develop within the electrolyte, causing concentration overpotentials and charge transport limitations. The improved ionic transport due to the channels in the electrodes effectively reduces concentration gradients in the electrolyte, enhancing CAM utilization across the cathode length.[39] At the highest simulated current (i = 8 mA/cm²), the capacity reaches its maximum value for a channel radius of 16 μm, with a significant increase of 0.6 mAh/cm² compared to the homogeneous electrode.

Figure 4(c) shows the Li-ion concentration in the electrolyte phase for channel radii of 0, 20, and 36 μm. As channel radius increases, concentration gradients decrease significantly across the cathode length, leading to more efficient charge transport in the electrolyte and reduced concentration overpotential.

Effect of transference number

The transference number of the electrolyte provides insight into the relative contributions of diffusion and migration to the overall ionic transport. A low transference number indicates diffusion-dominated Li-ion transport, while a high transference number indicates migration-dominated transport. Addressing

Research Article
doi.org/10.1002/batt.202300522
Chemistry Europe
European Chemical Societies Publishing

the need for efficient charge transport in the electrolyte and minimizing concentration overpotentials has led to intensive efforts in finding electrolytes with both high conductivity and transference number.[51–53] Inorganic SEs with high lithium conductivity and transference number are represented by transference numbers close to 1. Figure 5 illustrates the impact of increasing transference number on cell performance for electrodes with electrolyte channels at 8 mA/cm^2.

Figure 5(a) shows the simulated capacities for transference numbers between 0.3 and 1 at 8 mA/cm^2. As discussed in the previous section, structures with smaller channel radii exhibit high concentration gradients in the electrolyte, leading to significant concentration overpotentials. For these configurations, an increase in the transference number results in a significant capacity gain. However, ionic transport limitations are less pronounced for cathodes with larger channels, reducing the influence of transference number on cell performance.

As t_{Li}^{+} increases, capacities rise due to improved ionic transport. Concentration gradients across the cathode length diminish with increasing transference number (Figure 5(d)). The more efficient ionic transport has a direct impact on CAM utilization throughout the cathode (Figure 5(c)). While at $t_{Li}^{+} = 0.3$, the CAM near the current collector is less utilized, at $t_{Li}^{+} = 1$, utilization across the cathode length is almost constant.

Figure 5(b) shows the capacity gain due to electrolyte channels compared to the homogeneous electrode for varying transference numbers. As the transference number increases, concentration gradients in the electrolyte are reduced, diminishing capacity gains due to electrolyte channels. At high transference numbers ($t_{Li}^{+} > 0.7$), the perforated structures consistently show lower capacities than the non-perforated electrode at 8 mA/cm^2. On the one hand, this shows that the predominant benefit of electrolyte channels is enhanced diffusive transport, while the impact on migration is relatively minor. On the other hand, the results demonstrate that SEs with comparable ionic conductivity to LEs could pave the way toward efficient, high-performance cells with high power and energy density.

ASSB case

In the next step, we specifically focus on the influence of perforated cathode structures on ASSB performance with state-of-the-art SEs. We employ the SE parameters outlined in Table 2.

The primary goal of employing electrode structuring techniques is maximizing energy density at elevated current densities. Figure 6(a) demonstrates the impact of channel size on the energy density for current densities from 1 to 8 mA/cm^2. With increasing current density, the energy density decreases due to kinetic limitations, resulting in lower utilization of the CAM. Figure S3 shows the simulation results in terms of capacity. In contrast to the LIB case (cf. Figure 4), the cell performance is notably below the theoretical values even at low current densities. This is caused by the specific material parameters for the ASSB case. The SE has lower ionic conductivity compared to the LE. Additionally, we consider a reduced effective CAM diffusivity and exchange current density at the SE/CAM interface. Thus, despite the high transference number of the SE, CAM utilization is significantly lower than in the LIB case.

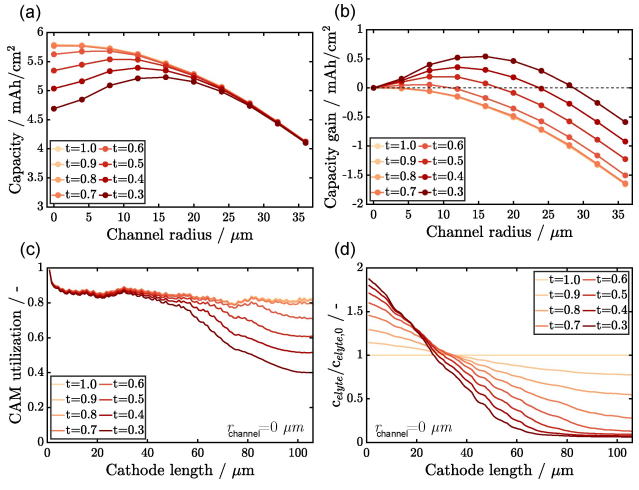

Figure 5. Effect of increasing transference number on electrochemical cell performance for perforated cathodes assuming parameters of the LIB case. (a) Impact of transference number on practical capacity at 8 mA/cm^2. (b) Impact of transference number on capacity gain compared to the non-perforated structure ($r_{channel} = 0$ μm) at 8 mA/cm^2. (c) Impact of transference number on the mean CAM utilization across the cathode thickness from separator to current collector for $r_{channel} = 0$ μm at 8 mA/cm^2. (d) Impact of transference number on the mean Li-ion concentration in the electrolyte across the cathode thickness from separator to current collector for $r_{channel} = 0$ μm at 8 mA/cm^2. The Li-ion concentration in the electrolyte is normalized by the initial Li-ion concentration.

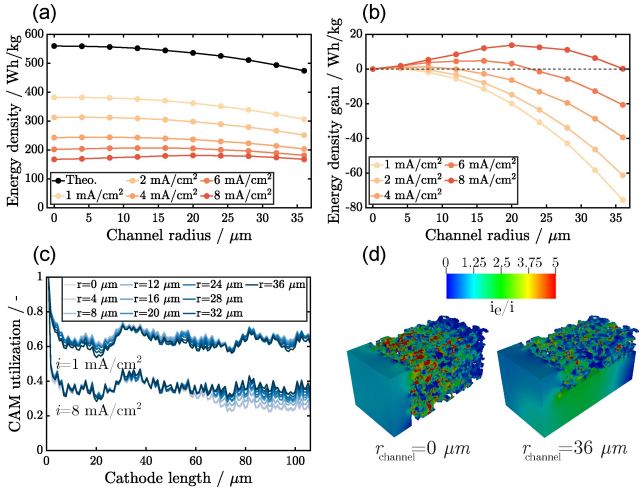

Figure 6. Effect of channel radius on electrochemical cell performance for the ASSB case. (a) Energy density for various current densities. The black line represents the theoretical energy density of the perforated structures. (b) Energy density gain of structures with channels at different current densities compared to the non-perforated structure ($r_{channel} = 0$ μm). (c) Impact of channel radius on the mean CAM utilization across the cathode thickness from separator to current collector at 1 mA/cm^2 and 8 mA/cm^2. (d) Current distribution in the electrolyte phase at the end of discharge for $r_{channel} = 0$ μm and $r_{channel} = 36$ μm and 8 mA/cm^2. Red regions indicate hot spots with high current density.

Research Article
doi.org/10.1002/batt.202300522
Chemistry Europe
European Chemical Societies Publishing

Figure 6(b) displays the energy density gain of cathodes with electrolyte channels relative to the homogeneous electrode. It is important to note that for the material system Li_6PS_5Cl/NMC811, the SE has a significantly lower density than the CAM. The reduced mass of structures containing more SE positively impacts energy density. Therefore, the calculated energy densities for cathodes with larger channels show a more favorable trend compared to the capacities depicted in Figure S3.

As discussed in the previous section, channels do not significantly enhance migration-dominated Li-ion transport. Still, they provide shorter conduction pathways and reduced effective tortuosity in the SE phase. Therefore, structures with electrolyte channels show higher energy densities at higher current densities than the homogeneous structure. However, the maximum energy density gain at 8 mA/cm^2 is modest (14 Wh/kg at $r_{channel} = 20$ µm).

Figure 6(c) displays the CAM utilization across the cathode length depending on channel size. Interestingly, at 1 mA/cm^2, CAM utilization decreases for larger channel sizes despite shorter conduction pathways. This can be explained by the reduced active areas in the structures with channels, resulting in larger interfacial currents and higher overpotentials. At 8 mA/cm^2, the shorter ionic conduction pathways in structures with channels lead to better CAM utilization at the current-collector side of the cathode. Figure 6(d) shows the current distribution in the electrolyte phase during discharge for $r_{channel} = 0$ µm and $r_{channel} = 36$ µm. Larger channels provide shorter ionic conduction pathways, resulting in lower peak currents and fewer hot spots.

Our simulations indicate that the potential of using cathodes with channels to improve ASSB performance is quite limited. Given the technical and economic challenges associated with manufacturing such electrodes for ASSBs, other concepts might be more promising.

Layered cathodes

Overview

As a second concept, we investigate a two-layer cathode design. The layered structures have a reduced CAM fraction (60 vol%) near the separator, enhancing ionic transport. Simultaneously, the layer close to the current collector has an increased CAM fraction (70 vol%), ensuring high CAM loading and enhanced effective electronic conductivity.

In our geometries, we vary the relative thickness of the separator layer f_{L60}, maintaining a consistent overall cathode thickness (cf. Section Structure generation). For reference, $f_{L60} = 0$ corresponds to a homogeneous cathode structure with 70 vol% CAM. In contrast, $f_{L60} = 1$ characterizes a homogeneous cathode with 60 vol% CAM.

Figure 7 shows the impact of increasing f_{L60} on effective ionic conductivity and theoretical capacity. As we extend layer L60, the effective ionic conductivity increases. However, the lower CAM fraction in the structures results in a decrease in theoretical capacity. Unlike the capacity, the effective ionic conductivity does not follow a linear trend. For larger f_{L60}, the increase in effective ionic conductivity becomes more pronounced.

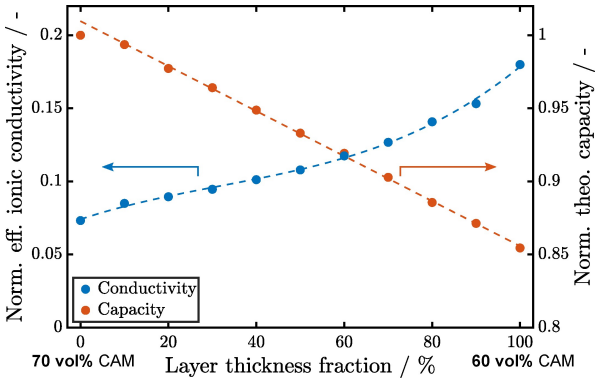

Figure 7. Impact of layer thickness fraction f_{L60} on effective ionic conductivity and theoretical capacity for a two-layer concept. The first layer adjacent to the separator has a CAM volume fraction of 60 vol%, while the second layer near the current collector has a CAM volume fraction of 70 vol%. The effective ionic conductivity is normalized with the bulk conductivity of the electrolyte. The theoretical capacity is normalized with the capacity of the homogeneous structure with 70 vol% CAM ($f_{L60} = 0$).

Electrochemical cell performance

Figure 8(a) illustrates the influence of the two-layer design on ASSB cell performance. Due to kinetic constraints, the simulated energy densities are significantly lower than the theoretical values, even at the smallest current density (1 mA/cm^2). Losses become more pronounced as the current density increases. The corresponding capacities are presented in Figure S4.

Figure 8 shows the gain in energy density (b) and capacity (c) resulting from a layer with higher SE content close to the current collector. At low current density (1 mA/cm^2), the capacity decreases with increasing f_{L60} owing to reduced theoretical capacity. This trend is not as pronounced in the energy density due to the lower specific mass of the SE.

At high current densities, the improved ionic transport in layered structures is more prominent, resulting in significantly improved cell performance compared to the non-layered structure with 70 vol% CAM. As the current density increases, the optimum configuration, balancing ionic transport and CAM loading, is shifted towards a higher thickness of the layer adjacent to the separator. At 4 mA/cm^2, the highest capacity is reached at $f_{L60} = 0.5$. At 6 and 8 mA/cm^2, maximum capacities are achieved at $f_{L60} = 0.8$ and $f_{L60} = 0.9$, respectively.

Given the lower density of Li_6PS_5Cl compared to NMC811, maximum energy density is reached at higher f_{L60}. At elevated current density (6 and 8 mA/cm^2), layered cathodes with $f_{L60} > 0.5$ can attain a gain in energy density exceeding 50 Wh/kg.

It is important to highlight that the orientation of the layers is critical for optimizing cell performance. Although a reverse structure, with a high CAM fraction near the separator and a

Research Article
doi.org/10.1002/batt.202300522
Chemistry Europe
European Chemical Societies Publishing

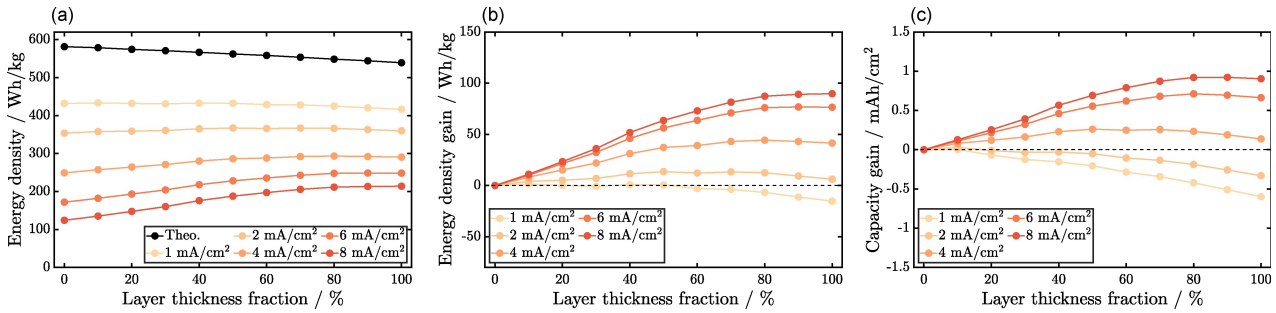

Figure 8. Influence of layer thickness fraction of the two-layered cathodes on electrochemical ASSB performance. (a) Energy density for current densities ranging from 1 to 8 mA/cm². The black line represents the theoretical energy density of the generated structures. (b) Energy density gain realized for the layered structures compared to a homogeneous cathode structure with 70% CAM ($f_{L60}=0$%). (c) Corresponding capacity gain.

low CAM fraction towards the current collector, has the same average properties, cell performance will be worse due to the high effective tortuosity near the separator. Figure S5 illustrates the simulated capacities for the reverse two-layer structures. The simulated capacities are significantly lower, especially at low and moderate f_{L60}.

Figure 9 provides insight into the effect of electrode layers on the charge transfer at $i=8$ mA/cm². Figure 9(a) shows the CAM lithiation at the lower cut-off voltage for structures with $f_{L60}=0$, 0.2, 0.5, 0.8, and 1. At $f_{L60}=0$, high CAM lithiation is primarily observed near the separator. Due to insufficient ionic transport in the SE phase, CAM utilization decreases significantly across the cathode length. As f_{L60} increases, the charge transport close to the separator significantly improves, resulting in fewer lithiation gradients. In the homogeneous structure with $f_{L60}=1$, the enhanced ionic transport enables almost constant lithiation across the cathode length. The generally low CAM utilization at 8 mA/cm² can be primarily attributed to the low Li mobility in NMC811, resulting in very low lithiation states in the particle centers.

Figure 9(b) demonstrates the effect of increasing f_{L60} on ionic transport represented by the electrochemical potential of Li-ions in the electrolyte. Due to lower ionic resistance, structures with high f_{L60} show reduced potential gradients in the SE phase across the cathode length, improving cell performance.

Enhanced ionic transport also reduces maximum local currents, as depicted in Figure 9(c). Practically, minimizing local currents and overpotentials are reported to mitigate local degradation phenomena.[54] For the layered configurations, elevated currents are more prominent at the interface between the two layers.

Interestingly, the layered structure with $f_{L60}=0.8$ and the homogeneous structure with 60 vol% CAM ($f_{L60}=1$) exhibit similar current and potential distributions. The two-layer

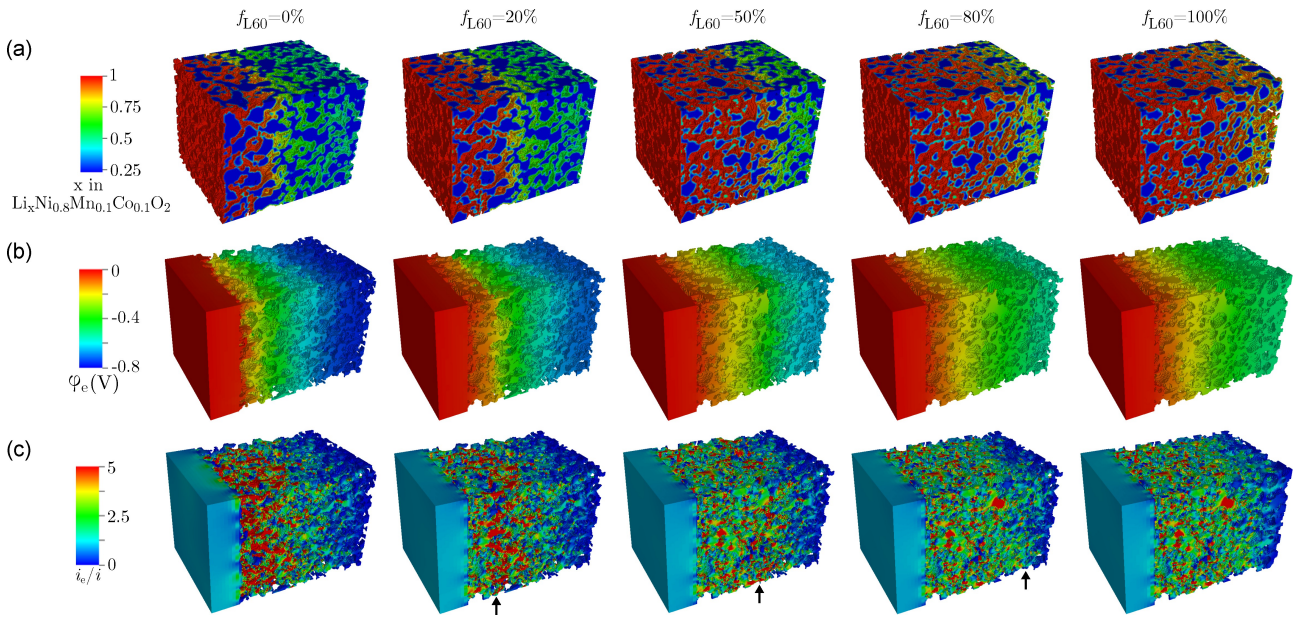

Figure 9. 3D simulation results for the two-layered structures with varying f_{L60} at the the lower cut-off voltage at $i=8$ mA/cm². (a) Influence of layer thickness fraction on CAM lithiation. (b) Influence of layer thickness fraction on electrochemical potential of Li-ions in the SE. (c) Influence of layer thickness fraction on ionic current in SE. Black arrows indicate the position of the interface between the layers L60 and L70.

Research Article
doi.org/10.1002/batt.202300522
Chemistry Europe
European Chemical Societies Publishing

structure shows only slightly lower lithiation of the CAM near the current collector while offering higher theoretical capacity.

Figure 10 shows the CAM utilization and cumulative capacity over the cathode length for layered structures with $f_{L60}=0.2$, 0.5, and 0.8. Across all current densities, a consistent trend in CAM utilization is observed. Generally, layer L60 has better utilization than layer L70 due to its lower effective tortuosity in the SE phase. The charge transfer kinetics govern the average utilization within each layer. CAM utilization drops more noticeably across the cathode length at high current densities due to ionic transport limitations. This decline is more pronounced in layer L70 compared to layer L60.

At the interface between both layers, a distinct peak in CAM utilization is evident. Over a length of approximately 2 μm, CAM utilization increases noticeably before decreasing to the levels characteristic of layer L70. Stacking during structure generation prevents a smooth transition between both layers and yields small CAM particles at the interface between the two layers. The higher CAM utilization is likely due to the decreased particle size compared to the rest of the structure, providing shorter diffusion pathways. Additionally, the discontinuity at the interface results in an increase of active surface area accessible for Li-ion intercalation, thereby contributing to the locally increased CAM utilization. It is worth noting that the peaks in CAM utilization between both layers become more prominent at higher current densities due to enhanced kinetics. In subsequent studies, applying advanced structure generators might help to ensure a smoother transition between layers L60 and L70.

At 1 mA/cm^2 (Figure 10(a)), all configurations exhibit consistently high CAM utilization. Given the relatively low current density, the overall capacity depends mainly on the CAM fraction in the structures. Thus, the increase in cumulative capacity is more significant in layer L70 than in layer L60. As a result, the cathode with $f_{L60}=0.2$ achieves a greater overall capacity compared to the structures with $f_{L60}=0.5$ and $f_{L60}=0.8$.

At 4 mA/cm^2 (Figure 10(b)), ionic transport limitations become more pronounced, causing a noticeable decrease in CAM utilization from the separator to the current collector. Additionally, the average CAM utilization in layer L70 is significantly lower than in layer L60. Among the depicted configurations, the structure with $f_{L60}=0.8$ has the highest CAM utilization across the entire cathode length. However, despite lower CAM utilization, the cathode with $f_{L60}=0.5$ shows slightly higher overall capacity due to the higher CAM loading.

At 8 mA/cm^2 (Figure 10(c)), CAM utilization decreases significantly across the cathode length. This reduction is more significant in layer L70 in comparison to layer L60. Consequently, the cathode with $f_{L60}=0.8$ shows significantly higher utilization, which despite its low CAM loading, results in higher capacities compared to the structures with $f_{L60}=0.2$ and $f_{L60}=0.5$.

Our simulation results show that the optimum configuration for the two-layer cathodes strongly depends on the operating conditions. In general, structures are favorable that show only minimal energy density loss at low current density compared to a homogeneous cathode with a high CAM fraction ($f_{L60}=0$). Simultaneously, at high current densities, these structures should approach the maximum energy density given by a homogeneous cathode with a low CAM fraction ($f_{L60}=1$). Structures with f_{L60} between 0.6 and 0.8 meet these criteria for the material system studied. However, note that the CAM fractions in the two layers are not optimized. Further refinement could enable higher energy densities, possibly favoring different configurations.

Conclusions and Outlook

The cell performance of ASSBs is limited by the low effective ionic conductivity observed in high-energy-density composite cathodes. Electrode structuring techniques offer the potential to enhance ionic charge transfer in the cathode while still allowing high CAM loading. In this work, we employ structure-resolved simulations to explore the impact of cathode structuring on cell performance. We determine the key factors governing cell performance by analyzing our simulation results for electrode designs with electrolyte channels and layers with varying electrolyte content. Moreover, we are able to identify optimal structures depending on operation conditions. Our simulations provide a quantitative description of cell performance and systematically investigate the effect of various structural parameters.

A promising concept primarily studied for conventional LIBs with liquid electrolytes is the use of electrolyte channels, providing pathways for fast ionic transport. Our simulation results show that channels wetted by a liquid electrolyte can

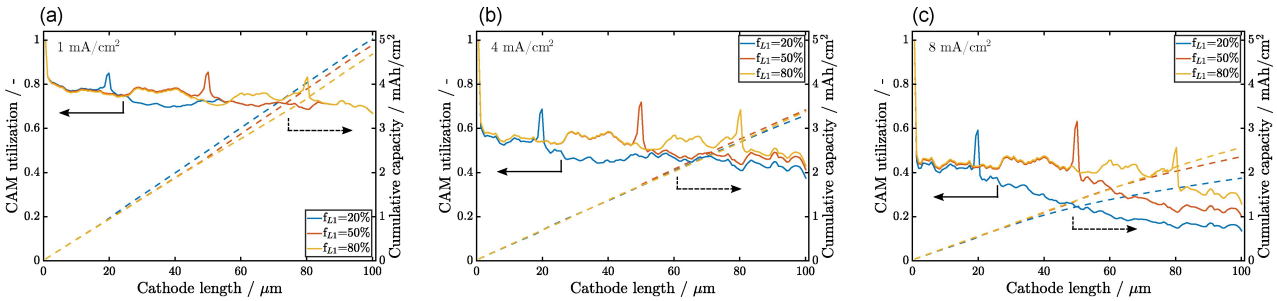

Figure 10. Influence of layer thickness fraction on mean CAM utilization and cumulative capacity across the cathode length. The separator is at 0 μm and the current collector at 100 μm. (a) $i=1$ mA/cm^2. (b) $i=4$ mA/cm^2. (c) $i=8$ mA/cm^2.

provide significantly increased capacities at elevated current densities. As channel size increases, concentration gradients in the electrolyte decrease, promoting more efficient ionic charge transport. At high current densities, improved transport outweighs the loss of CAM compared to unstructured electrodes.

However, most inorganic solid electrolytes are single-ion conductors with a transference number close to one. Therefore, concentration gradients in the SE are negligible except for space charge layers close to the CAM interface. As the transference number increases, the primary advantage of electrolyte channels – the reduction in concentration gradients – becomes less significant. Our simulation results show that, despite improved ionic transport through shorter transport pathways, electrolyte channels cannot significantly increase in cathode performance for ASSBs. This is attributed to less efficient charge transport compared to layered structures where the electrode structuring homogeneously reduces tortuosity in the primary direction of Li-ion transport. Additionally, larger electrolyte channels lead to reduced active areas for intercalation. This emphasizes that electrode designs which are effective for conventional LIBs must be rethought for ASSBs.

A promising strategy for ASSB development is the use of layered cathodes. Increasing the SE fraction at the separator side and CAM fraction at the current collector side makes it possible to achieve a cathode with high effective ionic and electronic conductivity while maintaining a high CAM loading. Our simulations investigate a two-layer concept with 60 vol% CAM at the separator and 70 vol% CAM at the current collector. We vary the thickness of both layers, keeping the overall cathode thickness constant. Our simulations indicate a significant potential for improved cell performance using layered cathodes. Increasing the thickness of the layer with lower CAM content at the separator reduces potential gradients in the electrolyte, resulting in decreased local current densities and overpotentials. Ideally, the capacity loss at low current densities due to reduced CAM fraction is minimal, while the capacity gain at high current densities from enhanced ionic transport is maximized. Depending on the materials and operating conditions, optimal performance was found when the layer at the separator starts to exceed 50% of the overall thickness. At the highest simulated current density of 8 mA/cm^2, the possible energy density achieved by the two-layer concept is approximately 90 Wh/kg.

Our simulation results encourage experimental studies focusing on layered cathodes for ASSBs. Increasing the number of layers to achieve a smoother gradient in CAM fraction across the cathode length will likely enhance cell performance further. Scalable manufacturing methods like tape-casting can produce multi-layer cathodes, making them particularly interesting for future cell designs.[45] Advanced deposition techniques such as powder aerosol deposition[55] (PAD) may pave the way for full gradient cathodes.

Particle size optimization offers another way to enhance charge transfer within the composite cathode. Similar to the approach explored in this study, the CAM particle size can be varied in the different layers.[56] Further simulation studies might explore a combined approach with gradients in both cathode composition and particle size using novel CAMs specifically designed for application in future ASSBs.

Computational Section

Simulation framework

For this study, we employ the Battery and Electrochemistry Simulation Tool (BEST), a finite volume implementation developed at DLR and Fraunhofer ITWM.[59] Within the simulation framework, the charge transport in the battery cell is calculated based on a set of coupled partial differential equations derived from the conservation equations for mass and charge.[19,57,58] Table 1 provides an overview of the governing equations.

In LEs, Li-ions are transported through migration and diffusion. Migration-based transport is driven by gradients in the electric field. The fraction of the resulting current carried by Li-ions is characterized by the transference number t_{Li}^{+}.[60] For LEs, t_{Li}^{+} is typically well below 1, suggesting that a substantial part of the current is carried by counter-ions moving opposite the Li-ions. As a result, concentration gradients develop in the electrolyte, leading to Li-ion transport by diffusion. In contrast, most SEs are considered single-ion conductors with $t_{Li}^{+}=1$. In this case, the system of equations in the electrolyte reduces to the Poisson equation with constant concentration within the electrolyte.

Material parameters

We simulate a LIB case with LE and an ASSB case with SE. The respective material parameters are taken from the literature. Table 2

Table 1. Governing equations used in BEST.[50,57,58]

Equation	Short description
Transport in active material	
$\frac{\partial c_{AM}}{\partial t} = -\nabla \cdot (-D_{AM} \nabla c_{AM})$	Mass balance
$0 = -\nabla \cdot i_{AM}$	Charge balance
$i_{AM} = -\sigma_{AM} \nabla \Phi_{AM}$	Electric current
Transport in electrolyte	
LE ($t_{Li}^{+} < 1$)	
$\frac{\partial c_e}{\partial t} = -\nabla \cdot \left(-D_e \nabla c_e + \frac{t_{Li}^{+} i_e}{F}\right)$	Mass balance
$0 = -\nabla \cdot i_e$	Charge balance
$i_e = -\kappa \nabla \Phi_e - \kappa_D \nabla c_e$	Ionic current
$\kappa_D = \frac{\kappa\left(t_{Li}^{+}-1\right)}{F}\left(\frac{\partial \mu_e}{\partial c_e}\right)$	
SE ($t_{Li}^{+} = 1$)	
$0 = -\nabla \cdot i_e$	Charge balance
$i_e = -\sigma_{Li}^{e} \nabla \Phi_e$	Ionic current
Interface between AM and electrolyte	
$i_{BV} = i_0\left[\exp\left(\frac{\alpha F}{RT}\eta\right) - \exp\left(-\frac{(1-\alpha)F}{RT}\eta\right)\right]$	Butler-Volmer current
$i_0 = i_{00}^{AM} c_e^{\alpha} c_{AM}^{\alpha}\left(c_{AM}^{max} - c_{AM}\right)^{1-\alpha}$	Exchange current density

Transport equations for the electrolyte phase simplify when assuming a SE with transference number of $t_{Li}^{+}=1$.

Research Article
doi.org/10.1002/batt.202300522

Table 2. Parameters of the electrochemical simulations.

Symbol	Value	Unit	Short description	Ref.
Li-metal				
U_0^{An}	0	*V*	Open circuit potential	–
σ_{Li}^{An}	1	*S*/cm	Electronic conductivity	–
i_0^{Li}	$2.59 \cdot 10^{-2}$	A/cm^2	Exchange current density	[20]
α^{Li}	0.5	–	Symmetry factor	[16]
NMC 811				
U_0^{CAM}	4.2	*V*	Open circuit potential*	[25]
$c_{Li}^{CAM,0}$	0.01131	mol/cm^3	Initial concentration of Li-ions	Calc.
$c_{Li}^{CAM,max}$	0.04903	mol/cm^3	Maximum concentration of Li-ions	Calc.
σ_{Li}^{CAM}	$8.83 \cdot 10^{-3}$	*S*/cm	Electronic conductivity*	[61]
D_{Li}^{CAM}	LE: $1.63 \cdot 10^{-12}$	cm^2/s	Li-ion diffusion coefficient*	[62]
	SE: $8.71 \cdot 10^{-13}$			
i_{00}^{CAM}	LE: $2.402 \cdot 10^{-2}$	$\frac{Acm^{2.5}}{mol^{1.5}}$	Exchange current density factor	Calc. from Ref. [62]
	SE: $1.5392 \cdot 10^{-3}$			
LE ($LiPF_6$)				
c_{Li}^{LE}	$1 \cdot 10^{-3}$	mol/cm^3	Concentration of Li-ions	–
κ_{Li}^{LE}	$9.4 \cdot 10^{-3}$	*S*/cm	Li-ion bulk conductivity*	[63]
D_{Li}^{LE}	$3.79 \cdot 10^{-6}$	cm^2/s	Li-ion diffusion coefficient*	[63]
t_{Li}^{+}	0.25	–	Transference number*	[63]
TDF	1.85	–	Thermodynamic factor*	[64]
l_{sep}	20	µm	Separator thickness	–
SE (Li_6PS_5Cl)				
c_{Li}^{SE}	0.036662	mol/cm^3	Concentration of Li-ions	Calc.
κ_{Li}^{SE}	$0.7 \cdot 10^{-3}$	*S*/cm	Li-ion bulk conductivity	[62]
t_{Li}^{+}	1	–	Transference number	–
l_{sep}	20	µm	Separator thickness	–
Operation				
U_{cut}	3.0	*V*	Cut-off voltage	–

Functional parameters are indicated by * and are given at initial conditions.

gives an overview of the parameters and corresponding references. Any deviations from these parameters are specified in the relevant section.

NMC811

In our simulations we consider the cathode active material NMC811. Material-specific parameters such as open circuit voltage, diffusion coefficient, and electric conductivity depend on the lithiation state and are included as functional parameters.[25,61,62]

In LIBs, microcracks that develop in NMC811 particles during cycling are invaded by the LE.[65] This results in shorter diffusion pathways in the CAM and increased active surface area. Consequently, the effective diffusion coefficient and charge transfer kinetics are higher compared to SEs.[62]

Liquid electrolyte

In our LIB simulations, we consider a LE with an initial concentration of 1 M $LiPF_6$ in EC:EMC (3:7). The respective material parameters are taken from the literature.[63,64] Ionic conductivity, diffusion coefficient, transference number, and thermodynamic factor are included as concentration-dependent parameters. In our simulations, we consider both the separator and CBD as homogenized media, characterized by effective transport parameters.[46] The

porous separator with a porosity of 50% is completely soaked with the LE. The effective conductivity is 50% of the bulk conductivity. Additionally, our input geometries include a CBD phase with 50% porosity[66,67] and an effective ionic conductivity of 12% of the bulk conductivity.

Solid electrolyte

For the SE, we consider the argyrodite Li_6PS_5Cl. The material parameters are taken from the literature.[62] Contrary to the LIB scenario, the separator is assumed to completely consist of SE. In particular, we consider a binder-free electrode.

Supporting Information

Additional references cited within the Supporting Information.[68,69]

Acknowledgements

The authors acknowledge support with computational resources provided by the state of Baden-Wurttemberg through bwHPC and the German Research Foundation (DFG) through grant no. INST 40/575-1 FUGG (JUSTUS 2 cluster). We gratefully acknowledge the financial support by the German Federal Ministry of Research and Education (BMBF) within the scope of the projects FestBatt2 (FKZ: 03XP0435A) and HiStructures (FKZ: 03XP0243D), as well as from the German Federal Ministry for Economic Affairs and Climate Action (BMWK) in the frame of the project structur.e (FKZ: 03ETE018D). The work of MN was funded by DFG under Project ID 390874152 (POLiS Cluster of Excellence, EXC 2154). The present paper contributes to the research performed at CELEST (Center for Electrochemical Energy Storage Ulm-Karlsruhe). Open Access funding enabled and organized by Projekt DEAL.

Conflict of Interests

There is no conflict of interest to declare.

Data Availability Statement

The data that support the findings of this study are available from the corresponding author upon reasonable request.

Keywords: all-solid-state batteries · composite cathode · continuum modeling · electrode structuring · microstructureresolved simulation

[1] Z. Li, A. Khajepour, J. Song, *Energy* **2019**, *182*, 824.
[2] B. Li, X. Gao, J. Li, C. Yuan, *Environ. Sci. Technol.* **2014**, *48*, 3047.
[3] L. A.-W. Ellingsen, B. Singh, A. H. Strømman, *Environ. Res. Lett.* **2016**, *11*, 054010.
[4] B. Diouf, R. Pode, *Renew. Energy* **2015**, *76*, 375.
[5] H. Tu, H. Feng, S. Srdic, S. Lukic, *IEEE Trans. Transp. Electrif.* **2019**, *5*, 861.
[6] M. Li, M. Feng, D. Luo, Z. Chen, *Cell Rep. Phys. Sci.* **2020**, *1*, 100212.
[7] Z. P. Cano, D. Banham, S. Ye, A. Hintennach, J. Lu, M. Fowler, Z. Chen, *Nat. Energy* **2018**, *3*, 279.
[8] T. Placke, R. Kloepsch, S. Dühnen, M. Winter, *J. Solid State Electrochem.* **2017**, *21*, 1939.
[9] M. Weiss, R. Ruess, J. Kasnatscheew, Y. Levartovsky, N. R. Levy, P. Minnmann, L. Stolz, T. Waldmann, M. Wohlfahrt-Mehrens, D. Aurbach, et al., *Adv. Energy Mater.* **2021**, *11*, 2101126.
[10] J. Janek, W. G. Zeier, *Nat. Energy* **2016**, *1*, 1.
[11] J. Janek, W. G. Zeier, *Nat. Energy* **2023**, *8*, 230.
[12] Y. Ren, T. Danner, A. Moy, M. Finsterbusch, T. Hamann, J. Dippell, T. Fuchs, M. Müller, R. Hoft, A. Weber, et al., *Adv. Energy Mater.* **2023**, *13*, 2201939.
[13] P. Minnmann, F. Strauss, A. Bielefeld, R. Ruess, P. Adelhelm, S. Burkhardt, S. L. Dreyer, E. Trevisanello, H. Ehrenberg, T. Brezesinski, et al., *Adv. Energy Mater.* **2022**, *12*, 2201425.
[14] L. Holzer, P. Marmet, M. Fingerle, A. Wiegmann, M. Neumann, V. Schmidt, *Tortuosity and microstructure effects in porous media: classical theories, empirical data and modern methods*, Springer **2023**.
[15] P. Minnmann, L. Quillman, S. Burkhardt, F. H. Richter, J. Janek, *J. Electrochem. Soc.* **2021**, *168*, 040537.
[16] M. Finsterbusch, T. Danner, C.-L. Tsai, S. Uhlenbruck, A. Latz, O. Guillon, *ACS Appl. Mater. Interfaces* **2018**, *10*, 22329.
[17] Y. J. Nam, D. Y. Oh, S. H. Jung, Y. S. Jung, *J. Power Sources* **2018**, *375*, 93.
[18] W. Zhang, D. A. Weber, H. Weigand, T. Arlt, I. Manke, D. Schröder, R. Koerver, T. Leichtweiss, P. Hartmann, W. G. Zeier, et al., *ACS Appl. Mater. Interfaces* **2017**, *9*, 17835.
[19] M. Clausnitzer, R. Mücke, F. Al-Jaljouli, S. Hein, M. Finsterbusch, T. Danner, D. Fattakhova-Rohlfing, O. Guillon, A. Latz, *Batteries Supercaps* **2023**, *6*, e202300167.
[20] A. Neumann, T. R. Hamann, T. Danner, S. Hein, K. Becker-Steinberger, E. Wachsman, A. Latz, *ACS Appl. Energy Mater.* **2021**, *4*, 4786.
[21] F. Strauss, T. Bartsch, L. de Biasi, A.-Y. Kim, J. Janek, P. Hartmann, T. Brezesinski, *ACS Energy Lett.* **2018**, *3*, 992.
[22] N. Kaiser, S. Spannenberger, M. Schmitt, M. Cronau, Y. Kato, B. Roling, *J. Power Sources* **2018**, *396*, 175.
[23] A. Bielefeld, D. A. Weber, J. Janek, *J. Phys. Chem. C* **2018**, *123*, 1626.
[24] A. Bielefeld, D. A. Weber, J. Janek, *ACS Appl. Mater. Interfaces* **2020**, *12*, 12821.
[25] A. Bielefeld, D. A. Weber, R. Rueß, V. Glavas, J. Janek, *J. Electrochem. Soc.* **2022**, *169*, 020539.
[26] L. Froboese, J. F. van der Sichel, T. Loellhoeffel, L. Helmers, A. Kwade, *J. Electrochem. Soc.* **2019**, *166*, A318.
[27] T. Shi, Q. Tu, Y. Tian, Y. Xiao, L. J. Miara, O. Kononova, G. Ceder, *Adv. Energy Mater.* **2020**, *10*, 1902881.
[28] M. Cronau, M. Duchardt, M. Szabo, B. Roling, *Batteries Supercaps* **2022**, *5*, e202200041.
[29] S. Yu, D. J. Siegel, *Chem. Mater.* **2017**, *29*, 9639.
[30] T. Ates, A. Neumann, T. Danner, A. Latz, M. Zarrabeitia, D. Stepien, A. Varzi, S. Passerini, *Adv. Sci.* **2022**, *9*, 2105234.
[31] P. Smyrek, J. Pröll, H. Seifert, W. Pfleging, *J. Electrochem. Soc.* **2015**, *163*, A19.
[32] M. Mangang, H. Seifert, W. Pfleging, *J. Power Sources* **2016**, *304*, 24.
[33] Y. Kim, A. Drews, R. Chandrasekaran, T. Miller, J. Sakamoto, *Ionics* **2018**, *24*, 2935.
[34] J. B. Habedank, L. Kraft, A. Rheinfeld, C. Krezdorn, A. Jossen, M. F. Zaeh, *J. Electrochem. Soc.* **2018**, *165*, A1563.
[35] J. B. Habedank, J. Kriegler, M. F. Zaeh, *J. Electrochem. Soc.* **2019**, *166*, A3940.
[36] L. Kraft, J. B. Habedank, A. Frank, A. Rheinfeld, A. Jossen, *J. Electrochem. Soc.* **2020**, *167*, 013506.
[37] K.-H. Chen, M. J. Namkoong, V. Goel, C. Yang, S. Kazemiabnavi, S. Mortuza, E. Kazyak, J. Mazumder, K. Thornton, J. Sakamoto, et al., *J. Power Sources* **2020**, *471*, 228475.
[38] J. Kriegler, L. Hille, S. Stock, L. Kraft, J. Hagemeister, J. B. Habedank, A. Jossen, M. F. Zaeh, *Appl. Energy* **2021**, *303*, 117693.
[39] V. De Lauri, L. Krumbein, S. Hein, B. Prifling, V. Schmidt, T. Danner, A. Latz, *ACS Appl. Energy Mater.* **2021**, *4*, 13847.
[40] V. Goel, K.-H. Chen, N. P. Dasgupta, K. Thornton, *Energy Storage Mater.* **2023**, *57*, 44.
[41] L. Gottschalk, C. Oertel, N. Strzelczyk, J. Müller, J. Krüger, W. Haselrieder, A. Kwade, *Energy Technol.* **2023**, *11*, 2200858.
[42] L.-C. Chen, D. Liu, T.-J. Liu, C. Tiu, C.-R. Yang, W.-B. Chu, C.-C. Wan, *J. Energy Storage* **2016**, *5*, 156.

[43] M. Wood, J. Li, Z. Du, C. Daniel, A. R. Dunlop, B. J. Polzin, A. N. Jansen, G. K. Krumdick, D. L. Wood III, *J. Power Sources* **2021**, *515*, 230429.
[44] C. Cheng, R. Drummond, S. R. Duncan, P. S. Grant, *J. Power Sources* **2020**, *448*, 227376.
[45] M. Rosen, M. Finsterbusch, O. Guillon, D. Fattakhova-Rohlfing, *J. Mater. Chem. A* **2022**, *10*, 2320.
[46] T. Knorr, S. Hein, B. Prifling, M. Neumann, T. Danner, V. Schmidt, A. Latz, *Energies* **2022**, *15*, 7821.
[47] M. Yamamoto, Y. Terauchi, A. Sakuda, M. Takahashi, *Sci. Rep.* **2018**, *8*, 1212.
[48] F. Hippauf, B. Schumm, S. Doerfler, H. Althues, S. Fujiki, T. Shiratsuchi, T. Tsujimura, Y. Aihara, S. Kaskel, *Energy Storage Mater.* **2019**, *21*, 390.
[49] M. Singh, J. Kaiser, H. Hahna, *J. Electrochem. Soc.* **2015**, *162*, A1196.
[50] T. Danner, M. Singh, S. Hein, J. Kaiser, H. Hahn, A. Latz, *J. Power Sources* **2016**, *334*, 191.
[51] K. M. Diederichsen, E. J. McShane, B. D. McCloskey, *ACS Energy Lett.* **2017**, *2*, 2563.
[52] E. Logan, J. Dahn, *Trends Chem.* **2020**, *2*, 354.
[53] P. Zhou, X. Zhang, Y. Xiang, K. Liu, *Nano Res.* **2023**, *16*, 8055.
[54] S.-K. Jung, H. Gwon, J. Hong, K.-Y. Park, D.-H. Seo, H. Kim, J. Hyun, W. Yang, K. Kang, *Adv. Energy Mater.* **2014**, *4*, 1300787.
[55] T. Nazarenus, Y. Sun, J. Exner, J. Kita, R. Moos, *Energy Technol.* **2021**, *9*, 2100211.
[56] R. Usiskin, J. Maier, *J. Electrochem. Soc.* **2020**, *167*, 080505.
[57] A. Latz, J. Zausch, *J. Power Sources* **2011**, *196*, 3296.
[58] A. Latz, J. Zausch, *Beilstein J. Nanotechnol.* **2015**, *6*, 987.
[59] https://www.itwm.fraunhofer.de/en/departments/sms/products-services/best-battery-electrochemistry-simulation-tool.html.
[60] J. Newman, N. P. Balsara, *Electrochemical systems*, John Wiley & Sons **2021**.
[61] R. Amin, Y.-M. Chiang, *J. Electrochem. Soc.* **2016**, *163*, A1512.
[62] R. Ruess, S. Schweidler, H. Hemmelmann, G. Conforto, A. Bielefeld, D. A. Weber, J. Sann, M. T. Elm, J. Janek, *J. Electrochem. Soc.* **2020**, *167*, 100532.
[63] A. Nyman, M. Behm, G. Lindbergh, *Electrochim. Acta* **2008**, *53*, 6356.
[64] J. Landesfeind, H. A. Gasteiger, *J. Electrochem. Soc.* **2019**, *166*, A3079.
[65] H.-H. Ryu, K.-J. Park, C. S. Yoon, Y.-K. Sun, *Chem. Mater.* **2018**, *30*, 1155.
[66] S. Vierrath, L. Zielke, R. Moroni, A. Mondon, D. R. Wheeler, R. Zengerle, S. Thiele, *Electrochem. Commun.* **2015**, *60*, 176.
[67] L. Zielke, T. Hutzenlaub, D. R. Wheeler, C.-W. Chao, I. Manke, A. Hilger, N. Paust, R. Zengerle, S. Thiele, *Adv. Energy Mater.* **2015**, *5*, 1401612.
[68] W. Xu, J. Wang, F. Ding, X. Chen, E. Nasybulin, Y. Zhang, J.-G. Zhang, *Energy Environ. Sci.* **2014**, *7*, 513.
[69] Materials data on Li_6PS_5Cl by Materials Project, 10.17188/1316731**2020**.

Manuscript received: November 9, 2023
Revised manuscript received: January 2, 2024
Accepted manuscript online: January 3, 2024
Version of record online: January 22, 2024